# Charged-current quasielastic neutrino scattering off nuclei with nucleon-nucleon short-range correlations*

Jian Liu (刘健)[1†] Qiang Su (苏强)[1] Qinglin Niu (牛清霖)[1] Lei Wang (王蕾)[2] Zhongzhou Ren (任中洲)[2‡]

[1]College of Science, China University of Petroleum (East China), Qingdao 266580, China
[2]School of Physics Science and Engineering, Tongji University, Shanghai 200092, China

**Abstract:** In recent years, neutrino-nucleus scattering has been extensively researched to investigate nuclear structures and interactions between neutrinos and nucleons. In this study, a charged-current quasielastic (CCQE) neutrino-nucleus scattering model is developed to explore the nuclear mean-field dynamics and short-range correlation effects. In this model, the effect of the nuclear structure is depicted using the scaling function $f(\psi)$, whereas the neutrino-nucleon interaction is represented by the elementary weak cross section $\sigma_0$. The results indicate that the double-differential cross section of the scattered muon is influenced by the energy $E$ and momentum $\mathbf{p}$ of the nucleon in the nuclei, and the total cross section depends primarily on the incident neutrino energy $E_\nu$. Furthermore, incorporating short-range correlations results in the flux-integrated differential cross sections in the high-$T_\mu$ region producing larger values, a longer tail, and achieving better experimental consistency. It eventually elucidates the physical relationship between the neutrino-nucleus scattering cross section and variation in the incident neutrino energy. This paper shares insights for the research on nucleon dynamics and presents detailed investigations of the neutrino-nucleus scattering mechanism.

**Keywords:** nucleon-nucleon short-range correlations, scaling function, charged-current quasielastic neutrino scattering

**DOI:** 10.1088/1674-1137/ade126 **CSTR:** 32044.14.ChinesePhysicsC.49104102

## I. INTRODUCTION

As a crucial tool in particle physics, nuclear physics, and cosmology, neutrino scattering plays a pivotal role in understanding fundamental particle interactions[1], revealing nucleon-nucleon short-range correlations (*NN*-SRCs) [2], and exploring cosmic evolution [3, 4]. Over recent decades, experiments on neutrino-nucleus scattering, including those conducted in CE$\nu$NS [5], NOMAD [6], MiniBooNE [7], MINOS [8], and T2K [9], have significantly advanced our understanding of the nuclear structure. Quasielastic neutrino scattering can be divided into two primary classifications: charged-current quasielastic (CCQE) neutrino scattering $\nu_l(\tilde{\nu}_l)+n(p)\to p(n)+\mu^-(\mu^+)$ and neutral-current quasielastic (NCQE) neutrino scattering $\nu_l(\tilde{\nu}_l)+n(p)\to\nu_l(\tilde{\nu}_l)+n(p)$ [10−12]. CCQE scattering is produced by the exchange of $W^\pm$ bosons, enabling a charge transfer at the interaction point. In contrast, in NCQE neutrino scattering, $Z^0$ bosons play a pivotal role, and no charge exchange occurs [13, 14]. CCQE neutrino scattering offers a unique perspective to study the nuclear internal dynamics owing to its charge-changing interaction between neutrinos and nucleons. In the scattering process, the incident neutrinos interact with individual nucleons, enabling the study of the nucleon interactions [15]. Therefore, in the CCQE domain, the changes in the nucleon momentum distribution (NMD) caused by nucleon correlations can be observed more effectively.

Plane-wave impulse approximation (PWIA) is an essential method for studying the neutrino-nucleus scattering. In the PWIA framework, the muon cross section can be expressed as a product of two parts: the elementary weak cross section $\sigma_0$ showing the neutrino scattering off a free nucleon and the scaling function $f(\psi)$ reflecting the nucleon distribution. The scaling function was first constructed based on the relativistic Fermi gas (RFG) model [16]. However, the classical RFG model cannot reproduce the experimental data well. Therefore, researchers have endeavored to develop scaling functions by introducing the nuclear dynamics. It is an effective method to de-

Received 8 April 2025; Accepted 4 June 2025; Published online 5 June 2025

* This work was supported by the National Natural Science Foundation of China (12475135, 12035011), by the Shandong Provincial Natural Science Foundation, China (ZR2020MA096), and by the Fundamental Research Funds for the Central Universities (22CX03017A).

† E-mail: liujian@upc.edu.cn

‡ E-mail: zren@tongji.edu.cn

rive the scaling function from the sophisticated nuclear structure model [17].

In past years, mean-field models based on energy density functionals (EDFs) have been used to investigate the nuclear properties [18−20]. Recently, theoretical and experimental studies have revealed the important role of *NN*-SRC, including the emergence of high momentum tails and diminished occupancy of low-lying nuclear states [21−23]. Therefore, the combination of mean-field and *NN*-SRC effects is expected to offer a theoretical explanation for neutrino-nucleus scattering. There are multiple approaches to introduce *NN*-SRC effects, and the light-front dynamics (LFD) approach is a feasible choice [24]. The LFD method calculates the NMD of the correlation part $n_{\rm corr}(p)$ by empirically rescaling the high-momentum components of the NMDs of the deuteron [25]. Examining the momentum distribution of neutrons is more challenging than that of protons, primarily because of their electrical neutrality. This study aims to explore the properties of neutrons through the neutrino-neutron reaction $\nu_l + n \to p + \mu^-$. Given that neutrinos interact with neutrons only via weak forces, CCQE neutrino scattering presents distinct advantages in probing the momentum distribution of neutrons.

This main work of this study is organized as follows. First, we investigate the spectral function $S(\mathbf{p},E)$, which represents the joint probability distribution for finding a nucleon in the target nucleus with momentum $\mathbf{p}$ and removal energy $E$. For calculating $S(\mathbf{p},E)$, the mean-field component is calculated from the axially deformed Hartree-Fock-Bogoliubov (HFB) [26] model, whereas the correlation part is introduced through the LFD method. Subsequently, based on the spectral function $S(\mathbf{p},E)$, the scaling function $f(\psi)$is derived to effectively represent the structural information of the target nucleus. Finally, we focus on building the CCQE neutrino-nucleus scattering model, in which the elementary weak cross section $\sigma_0$is calculated based on the nucleon form factor and the nuclear structure is introduced through the scaling function $f(\psi)$. The influence of the *NN*-SRC on the neutron momentum distribution is evaluated using experimental observations.

This paper is organized as follows: In Sec. II, we present the scaling function $f(\psi)$ and provides the corresponding formulas for CCQE neutrino-nucleus scattering. In Sec. III, the results of the neutrino scattering cross sections are presented and discussed. Finally, a summary is presented in Sec. IV.

## II. THEORETICAL FRAMEWORK

This section is divided into three parts. First, we present the theoretical formulas for the CCQE neutrino-nucleus scattering cross section. Second, the scaling function $f(\psi)$ reflecting the nuclear structure information is constructed using the spectral function $S(\mathbf{p},E)$. Finally, the spectral function $S(\mathbf{p},E)$ is derived using the HFB theory and LFD method.

### A. CCQE neutrino cross section

CCQE neutrino scattering refers to the process $\nu_l + n \to p + \mu^-$, where a neutrino interacts with a target nucleus, resulting in the emission of a single muon. In this paper, we denote the energy of the incoming neutrino as $E_\nu$and the kinetic energy of the outgoing muon as $T_\mu$. The mass of the muon is $m'_\mu$ and total space scattering angle is denoted as $\Omega'$. The momentum transfer is denoted by $q$, and the energy transfer is denoted by $\omega$.

The neutrino double-differential cross section is expressed as the product of the elementary weak scattering cross section $\sigma_0$ and structure function $\mathcal{F}_+^2$

$$\frac{\mathrm{d}^2\sigma}{\mathrm{d}\Omega'\mathrm{d}T_\mu} = \sigma_0 \mathcal{F}_+^2, \tag{1}$$

where $\sigma_0$ represents the scattering cross section for neutrino interactions with a free nucleon.

$$\sigma_0 = \frac{G^2\cos^2\theta_c}{2\pi^2} k' T_\mu \cos^2\frac{\tilde{\theta}}{2}. \tag{2}$$

Here, $G = 1.166\times10^{-11}\mathrm{MeV}^{-2}$ describes the strength of the weak interaction, and the Cabibbo angle $\cos\theta_c = 0.975$ preserves the universality of the weak interaction. $k'$ is the momentum of the outgoing muon. The generalized scattering angle $\tilde{\theta}$ in Eq. (2) is [27]

$$\tan^2\frac{\tilde{\theta}}{2} = \frac{|Q^2|}{(E_\nu + T_\mu)^2 - q^2}, \tag{3}$$

where $Q^2 = \omega^2 - q^2$.

The structure function $\mathcal{F}_+^2$ in Eq. (1) contains the neutron momentum distributions, neutron energy distributions, nucleon form factors, and other nuclear structure details. $\mathcal{F}_+^2$ can be presented as a generalized Rosenbluth decomposition having charge-charge, charge-longitudinal, longitudinal-longitudinal, and two types of transverse responses [27].

$$\mathcal{F}_+^2 = \widehat{V}_{CC}R_{CC} + 2\widehat{V}_{CL}R_{CL} + \widehat{V}_{LL}R_{LL} + \widehat{V}_T R_T + 2\widehat{V}_{T'}R_{T'}, \tag{4}$$

where the kinematical factors $\hat{V}_K (K = CC, CL, LL, T, T')$ originate from the leptonic tensor. The response function $R_K$ in Eq. (4) is expressed as

$$R_K = \mathcal{N}\Lambda_0 U_K f(\psi), \quad K = CC, CL, LL, T, T', \tag{5}$$

where $\mathcal{N}$ is the neutron number. $\Lambda_0$ and $U_K$ in Eq. (5) are

the response factor and single-nucleon responses, which can be referred from [28]. $f(\psi)$ is the $\psi$ scaling function that contains the nuclear structure information. The detailed description is provided in the next subsection.

After obtaining the double-differential cross section $\mathrm{d}^2\sigma/\mathrm{d}\Omega'\mathrm{d}T_\mu$, we evaluate the flux differential cross section for the CCQE process averaged over the neutrino flux $\Phi(E_\nu)$

$$\frac{\mathrm{d}^2\sigma}{\mathrm{d}T_\mu \mathrm{d}\cos\theta_\mu} = \frac{1}{\Phi_{\rm tot}} \int \left[\frac{\mathrm{d}^2\sigma}{\mathrm{d}T_\mu \mathrm{d}\cos\theta_\mu}\right]_{E_\nu} \Phi(E_\nu)\mathrm{d}E_\nu, \quad (6)$$

where $\theta_\mu$ is the scattering angle of the outgoing muon. The neutrino flux $\Phi(E_\nu)$ represents the probability of the neutrinos interacting with other matter at different incident energies, and $\Phi_{\rm tot}$ is the total integrated neutrino flux factor [7, 29, 30].

By integrating over the scattering angle $\theta_\mu$ and incident neutrino energy $E_\nu$ in the double-differential cross section of Eq. (1), we can obtain the differential cross section as a function of the outgoing muon kinetic energy $T_\mu$, as follows:

$$\left\langle\frac{\mathrm{d}\sigma}{\mathrm{d}T_\mu}\right\rangle = \frac{1}{\Phi_{\rm tot}} \int \Phi(E_\nu) \int \left[\frac{\mathrm{d}^2\sigma}{\mathrm{d}T_\mu \mathrm{d}\cos\theta_\mu}\right]_{E_\nu} \mathrm{d}\cos\theta_\mu \mathrm{d}E_\nu. \quad (7)$$

Similarly, the differential cross section as a function of $\theta_\mu$ can be obtained by integrating over both the outgoing muon kinetic energy $T_\mu$ and incident neutrino energy $E_\nu$

$$\left\langle\frac{\mathrm{d}\sigma}{\mathrm{d}\cos\theta_\mu}\right\rangle = \frac{1}{\Phi_{\rm tot}} \int \Phi(E_\nu) \int \left[\frac{\mathrm{d}^2\sigma}{\mathrm{d}T_\mu \mathrm{d}\cos\theta_\mu}\right]_{E_\nu} \mathrm{d}T_\mu \mathrm{d}E_\nu. \quad (8)$$

Finally, the total cross section $\sigma_T$ of neutrino-nucleus scattering is expressed by integrating over $\theta_\mu$ and $T_\mu$ in the double-differential cross section, as follows:

$$\sigma_T(E_\nu) = \iint \left[\frac{\mathrm{d}^2\sigma}{\mathrm{d}T_\mu \mathrm{d}\cos\theta_\mu}\right]_{E_\nu} \mathrm{d}T_\mu \mathrm{d}\cos\theta_\mu. \quad (9)$$

### B. $\psi$ scaling function in CCQE cross section

Scaling method is a powerful tool to study neutrino scattering in the quasielastic region, which elucidates the dynamics of the neutrino interactions with the nucleons inside the nucleus [31]. The $\psi$ scaling function provides critical insights into the target nucleus, capturing the distributions of momentum and energy among its nucleons. We introduce a kinematical variable, namely, the scaling variable $\psi$, which is solely dependent on the momentum transfer $q$ and energy transfer $\omega$ [32], as follows:

$$\psi = \frac{1}{\sqrt{\xi_F}} \frac{\lambda - \tau}{\sqrt{(1+\lambda)\tau + \kappa\sqrt{\tau(1+\tau)}}}, \quad (10)$$

where $\lambda \equiv \omega/2m_n$ and $\tau \equiv \kappa^2 - \lambda^2$ [17]. $m_n$ is the neutron mass. $\kappa$ and $\xi_F$ are the dimensionless fermi kinetic energy and transfer momentum factor, respectively, as defined in [28]. The scaling function can be derived from the structure functions [33] as

$$F(q,\psi) = 2\pi \int_{E_{\rm min}}^{E_{\rm max}(q,\psi)} \mathrm{d}E \int_{P_{\rm min}(q,\psi,E)}^{P_{\rm max}(q,\psi,E)} \mathrm{d}p S(p,E) p, \quad (11)$$

where $S(\mathbf{p},E)$ is the neutron spectral function, which is described in detail in Sec. II.C. Through energy conservation in the scattering process, the upper and lower limits of the energy integration in Eq. (11) are defined as

$$E_{\rm min} = M_{A-1} + m_n - M_A, \quad (12a)$$

$$E_{\rm max} = M_A^* - M_A, \quad (12b)$$

where $E_{\rm min}$ denotes the single-neutron separation energy and $M_A^*$ is the effective mass of the system composed of the residual nucleons. We further introduce momentum conservation in the CCQE process as

$$\omega + M_A = \sqrt{{m_n}^2 + (\mathbf{k}+\mathbf{q})^2} + \sqrt{M_{A-1}^{*2} + \mathbf{k}^2}, \quad (13)$$

where the angle between $\mathbf{k}$ and $\mathbf{q}$ ranges from 0° to 180°. By substituting the angles of 0° and 180° into Eq. (13), we obtain the upper and lower limits of the momentum integration in Eq. (11). The upper and lower bounds of the momentum integral can be found in our previous study [34].

At a large $q$, the scaling function depends only on a single kinematic variable $\psi$, and we can obtain the dimensionless scaling function $f(\psi)$ of Eq. (5) as [12]

$$f(\psi) = F(q,\psi) \times p_F. \quad (14)$$

In Eq. (14), $p_F$ denotes the Fermi momentum of the nucleus. Because of the CCQE process, where neutrinos react only with neutrons, the spectral function for $f(\psi)$ calculations considers only the energy and momentum distributions of the neutrons.

### C. Nuclear spectral function

The neutron spectral function $S(\mathbf{p},E)$ in Eq. (12) represents the probability of finding a neutron with momentum $\mathbf{p}$ and removal energy $E$ in the nuclei [35]. In this paper, the calculations of the spectral function

$S(\mathbf{p},E)$ are divided into two parts: the mean-field (MF) part $S(\mathbf{p},E)$ and correlation component $S_{\rm corr}(\mathbf{p},E)$ [22], as follows:

$$S(\mathbf{p},E)=S_{\rm MF}(\mathbf{p},E)+S_{\rm corr}(\mathbf{p},E). \tag{15}$$

The MF part $S_{\rm MF}(\mathbf{p},E)$ is dominated by the single-neutron properties at a low energy and low momentum.

$$S_{\rm MF}(\mathbf{p},E)=\sum_i C_i n_i(\mathbf{p})L_i(E-E_i), \tag{16}$$

where $C_i$ is the corresponding occupation number of the single-neutron state $i$. The Lorentzian function $L_i$ describes the finite width in energy dependence and $E_i$ is the eigenvalue of the energy of the state $i$. The detailed parameters of $E_i$ and their values are sourced from Refs. [22] and [36]. The single-neutron momentum distribution $n_i(\mathbf{p})$ is obtained by applying the Fourier transform to the single-particle Hartree-Fock nucleon wave function from $r$-space to $p$-space [25]. The wave function is calculated using HFB2.0 code [37], which allows for axially symmetric deformations.

The correlation component $S_{\rm corr}(\mathbf{p},E)$ in Eq. (15) can be obtained from

$$S_{\rm corr}(\mathbf{p},E)=n_{\rm corr}(\mathbf{p})\frac{m_n}{|\mathbf{p}|}\sqrt{\frac{\alpha}{\pi}}\left[\exp\left(-\alpha\mathbf{p}_{\rm min}^2\right)-\exp\left(-\alpha\mathbf{p}_{\rm max}^2\right)\right], \tag{17}$$

where $m_n$ is the neutron mass and $\alpha=3/[4\langle\mathbf{p}^2\rangle(A-2)/(A-1)]$ [38]. $\mathbf{p}_{\rm min}$ and $\mathbf{p}_{\rm max}$ in Eq. (17) are the lower and upper limits of the center-of-mass momentum.

$$\mathbf{p}_{\rm min}^2=\left\{\frac{A-2}{A-1}|\mathbf{p}|-\sqrt{2m_n\frac{A-2}{A-1}\left[E-E^{(2)}\right]}\right\}^2, \tag{18a}$$

$$\mathbf{p}_{\rm max}^2=\left\{\frac{A-2}{A-1}|\mathbf{p}|+\sqrt{2m_n\frac{A-2}{A-1}\left[E-E^{(2)}\right]}\right\}^2, \tag{18b}$$

where $E^{(2)}$ is the two-nucleon separation energy. To calculate the momentum distribution $n_{\rm corr}(\mathbf{p})$ in Eq. (17), we adopted the light-front dynamics (LFD) method, where the one-boson-exchange model is applied to the nucleon-nucleon interaction and the parameters are obtained from the Bonn potential [24]. The LFD method calculates the correlation part $n_{\rm corr}(\mathbf{p})$ by empirically rescaling the high-momentum component of the momentum distribution of the deuteron, as follows:

$$n_{\rm corr}(\mathbf{p})=N_\tau\mathcal{N}C_A\left[n_2(\mathbf{p})+n_5(\mathbf{p})\right], \tag{19}$$

where the two components $n_2(\mathbf{p})$ and $n_5(\mathbf{p})$ are deduced from the LFD wave functions [25]. Within the LFD framework, $n_2$ originates primarily from the tensor force interactions and exhibits dominance in the range $1.5<\mathbf{p}<3.0$ fm$^{-1}$, whereas $n_5$ arises predominantly from the $\pi$-meson exchange and contributes primarily at a higher momentum $\mathbf{p}>2.5$ fm$^{-1}$. The scaling factor $C_A$ in Eq. (19) is the ratio of the high-momentum components between the deuteron and target nuclei. $N_\tau$ is the normalization coefficient. The detailed formula for calculating the NMD and spectral function can be found in our previous study [25, 35].

## III. NUMERICAL RESULTS AND ANALYSIS

In this section, the NMDs and spectral functions are examined using the HFB model and the LFD method. Based on these analyses, the $\psi$-scaling function is constructed to investigate the CCQE neutrino scattering process. In addition, we explore the CCQE scattering cross sections, including the double-differential, flux-integrated, and total cross sections, using the $\psi$-scaling function.

### A. Momentum distributions, spectral functions, and $\psi$-scaling function

First, we present the results for the nucleon momentum distributions $n(p)$, neutron spectral function $S(p,E)$, and $\psi$-scaling function $f(\psi)$ of $^{12}$C. The corresponding nucleon single-particle wave functions in $p$-space are computed from the axially deformed HFB model using the SLy4 parameter set. The correlation part spectral function $S_{\rm corr}(p,E)$ is obtained using the LFD method; the correlation strength is $C_A=4.5$, as specified in Eq. (19). When calculating the $\psi$-scaling function, we use the

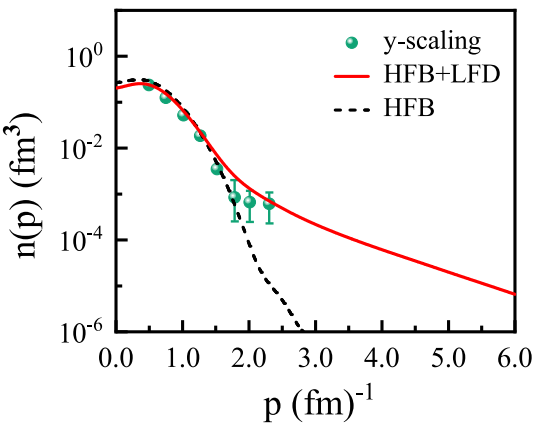


**Fig. 1.** (color online) Total momentum distribution $n(p)$ of $^{12}$C for the configuration $\beta=-0.1$, calculated from the deformed HFB model and the LFD method. The green balls represent the $n(p)$ obtained from $y$-scaling analyses on $(e,e')$ cross sections [33].

Fermi momentum $p_F = 1.1$ fm$^{-1}$ [14, 39].

In Fig. 1, we compare the total NMDs $n(p)$ calculated using the HFB and HFB+LFD methods for the configuration ($\beta = -0.1$). $\beta$ represents the quadrupole deformation of the nucleus [37]. The black dashed line depicts the $n(p)$ calculated using the HFB model, whereas the red solid line represents the $n(p)$ obtained using the HFB+LFD method. The NMDs extracted from the $y$ scaling analyses on $(e,e')$ experiments are also provided in this figure for comparison [33]. From Fig. 1, we can see that the HFB calculations provide accurate descriptions of the NMD under the Fermi momentum $p_F$. For $p > p_F$, $n(p)$ from the MF model decreases rapidly and diverges from the experimental data. By introducing the *NN*-SRC contributions with the LFD method, the tail values of $n(p)$ are enhanced, yielding a 24% proportion of high-momentum neutrons above the Fermi surface. This result shows excellent agreement with the $y$-scaling analysis measurements. Through contrastive analysis, the LFD results in Fig. 1 are found to be in agreement with the calculations from the realistic nucleon-nucleon interactions, such as Nijmegen-I, -II, -Reid, Argonne $v_{18}$, and Paris *NN* potentials [40].

Using the methods in Sec. II.C, the spectral function $S(p, E)$ can be calculated by considering the $n(p)$ of both the MF and correlation components. Figure 2 presents the logarithm of the neutron spectral functions $S(p, E)$ of $^{12}$C to show the effect of *NN*-SRC. It can be seen that in the regions of $E > 0.05$GeV and $p > 2.0$ fm$^{-1}$, $S(p, E)$ is predominantly attributed to the contributions from *NN*-SRC, which has no shell structure and appears in a smooth ridge. Unlike the *NN*-SRC part, the different single-particle states in the MF region (enclosed by a curve) can be clearly distinguished in Fig. 2. It should be noted that the nuclear deformation affects the momentum distribution $n(p)$ by modifying the single-particle energy levels, thereby affecting the number of nucleons participating in the scattering processes, which has been addressed in our earlier study [35].

The scaling function describes the relationship between the calculations of the nuclear structure and the CCQE neutrino scattering process, as explained in Sec. II.B. In this part, based on the neutron spectral function $S(p, E)$ in Fig. 2, the $\psi$-scaling function $f(\psi)$ is calculated by integrating $S(p, E)$ over the energy $E$ and momentum $p$. In Fig. 3, two $\psi$-scaling functions from the HFB and HFB+LFD models are presented with the normalization $\int f(\psi)\mathrm{d}\psi = 1$. To further strengthen the credibility of our models, we also calculate and include $f(\psi)$ from the Coherent Density Fluctuation Model (CDFM) and the experimental $f(\psi)$ extracted from electron scattering experiments [41]. As shown in this figure, the two theoretical $f(\psi)$, obtained with and without *NN*-SRC, can reflect the overall trend of the experimental data.

After considering *NN*-SRC, the $\psi$-scaling function

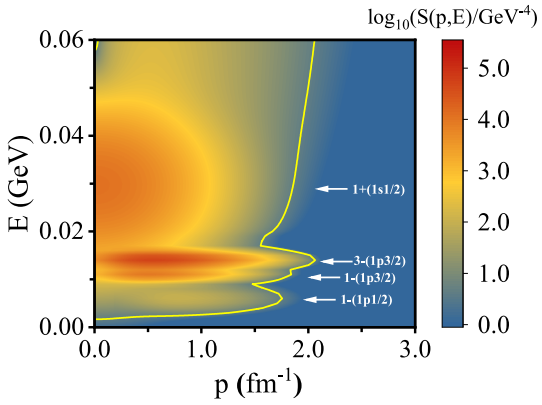


**Fig. 2.** (color online) Neutron spectral functions $S(p, E)$ of $^{12}$C for the configuration $\beta = -0.1$, calculated from the deformed HFB model and the LFD method. The logarithm of $S(p, E)$ is presented to highlight the *NN*-SRC part, and the region enclosed by the curve describes the MF contribution.

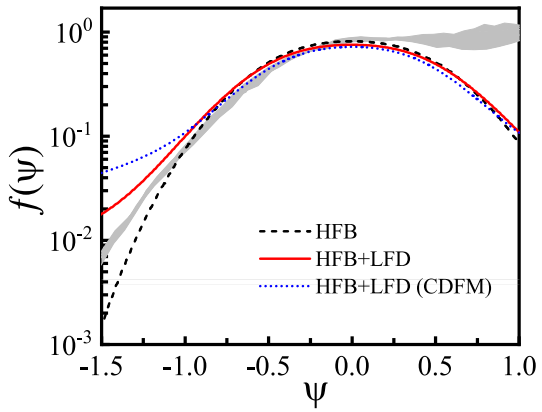


**Fig. 3.** (color online) Scaling function $f(\psi)$ for $^{12}$C, obtained using the HFB, HFB + LFD, and HFB+LFD (CDFM) models at $q$=1000 MeV/c with the normalization $\int f(\psi)\mathrm{d}\psi = 1$. The experimental data (gray area) are from Ref. [41].

demonstrates different behaviors at the peak position and in the negative-$\psi$ region. At the peak position of $f(\psi)$, the result of the HFB+LFD model is lower than that of the HFB model. In the tail of $f(\psi)$, the values from the HFB+LFD model are higher than those from the HFB model, especially in the region $\psi < -1.0$. This indicates that *NN*-SRC mainly contributes to the low and high energy tails of $f(\psi)$. Additionally, when compared with the HFB model, $f(\psi)$with *NN*-SRC exhibits asymmetry. This reflects that the strong interactions between the particles induce asymmetry in the energy distribution. To enhance the credibility of our results, the HFB+LFD results are compared with those from the CDFM. As shown in Fig. 3, our results are consistent in behavior with those of the CDFM, and both align closely with the experimental data.

From Fig. 3, although the inclusion of the *NN*-SRC effects improves the behavior of $f(\psi)$, minor discrepan-

cies persist between the theoretical predictions and experimental data. This is because the model neglects certain complex many-body effects, including but not limited to two-particle-two-hole (2p-2h) excitations and meson-exchange currents (MECs) [42–44]. The 2p-2h states, describing short-range correlations as transient high-momentum nucleon pairs, introduce a non-independent particle motion that significantly alters the nucleon momentum distribution, with dominant contributions in the negative-$\psi$ region [45]. MEC arising from non-local interactions mediated by virtual pions and other particles between nucleons primarily induces further enhancement of the $f(\psi)$ scaling function in the negative-$\psi$ region [46].

### B. CCQE neutrino scattering cross sections

In this subsection, we utilize the scaling function $f(\psi)$ to study the CCQE neutrino scattering cross sections and analyze the effect of the nuclear structure on the differential and total cross sections.

After obtaining the $\psi$-scaling function, the double-differential cross section $\mathrm{d}^2\sigma/\mathrm{d}\Omega'\mathrm{d}T_\mu$ of the CCQE neutrino scattering of $^{12}$C is computed by decomposing the cross sections into the product of the elementary weak scattering cross section $\sigma_0$ and structure function $\mathcal{F}_+^2$, as described in Sec. II.A. The corresponding results calculated from the HFB and HFB+LFD models are shown in Fig. 4. The horizontal axis represents the kinetic energy of the emitted muons, denoted as $T_\mu$. Figure 4 displays $\mathrm{d}^2\sigma/\mathrm{d}\Omega'\mathrm{d}T_\mu$ at the incident neutrino energies of $E_\nu = 0.4$, 0.7, 1.0, and 1.3 GeV and scattering angle $\theta_\mu = 30°$.

In Fig. 4, three distinct characteristics of the cross sections can be observed. The peak of $\mathrm{d}^2\sigma/\mathrm{d}\Omega'\mathrm{d}T_\mu$ corresponds to the position where the scaling function $\psi = 0$ in $f(\psi)$. The position of this peak indicates that neutrinos are scattered by neutrons with momentum $p = 0$. In addition, as $E_\nu$ increases, the location of the peak shifts toward a high $T_\mu$. This is because the increase in $E_\nu$ leads to a corresponding rise in $T_\mu$. Finally, the peak position of the cross section initially increases and then decreases with increasing $E_\nu$. This behavior is linked to the interactions between neutrinos and neutrons. A detailed discussion of the total cross section is presented later.

It can also be observed in the four panels of Fig. 4 that after introducing *NN*-SRC, the values of $\mathrm{d}^2\sigma/\mathrm{d}\Omega'\mathrm{d}T_\mu$ increase in the high-$T_\mu$ region. This is because the correlations increase the number of high-$p$ neutrons in Fig. 1. In comparison with the MF nucleons, the contribution of these high-$p$ nucleons becomes more pronounced at higher outgoing energies [34]. Furthermore, the value of $\mathrm{d}^2\sigma/\mathrm{d}\Omega'\mathrm{d}T_\mu$ at the peak position decreases in the four

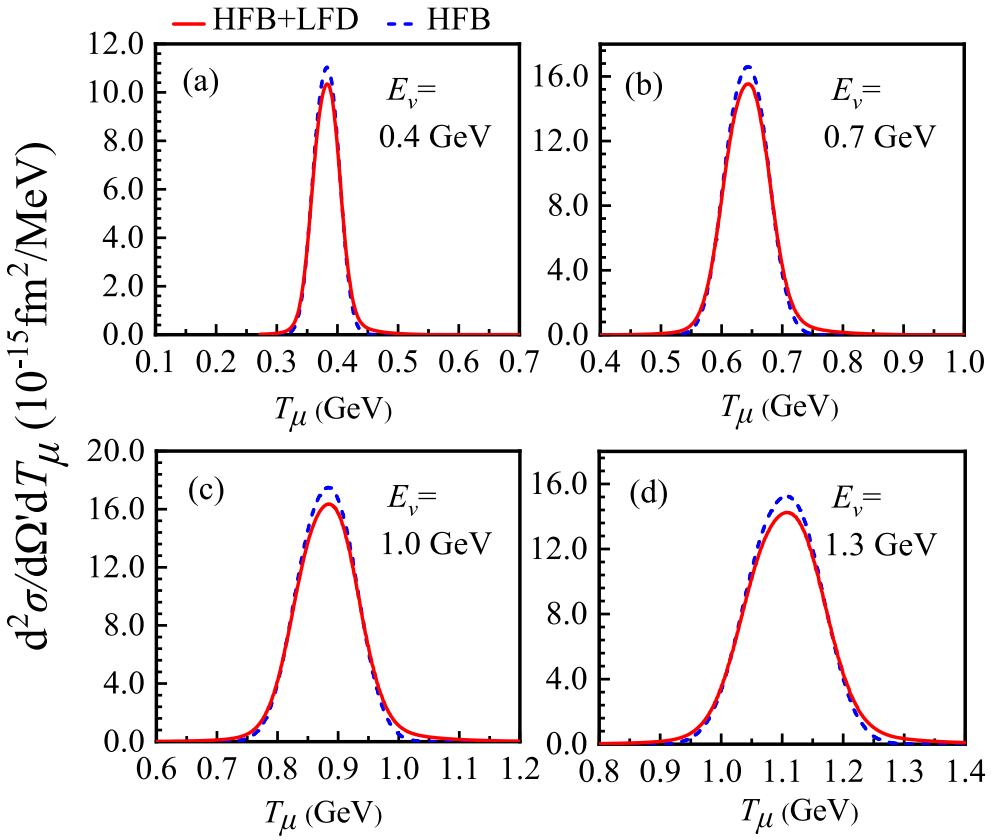


**Fig. 4.** (color online) Double-differential cross sections of the reaction $^{12}\mathrm{C}\left(\nu_\mu,\mu^-\right)$ for different incident neutrino energies $E_\nu$ at scattering angle $\theta_\mu = 30°$.

panels of Fig. 4 after considering the contribution of *NN*-SRC. For a fixed incident energy $E_\nu$ and scattering angle $\theta_\mu$, not all neutrons can participate in the CCQE scattering process, and some of the neutrons are excluded owing to the requisite conditions of energy and momentum in Eq. (11). Therefore, after incorporating *NN*-SRC, the cross section is smaller than the cross sections with only MF contributions.

The quasielastic $^{12}$C $(\nu_\mu,\mu^-)$ flux-integrated differential cross section $\mathrm{d}^2\sigma/\mathrm{d}\cos\theta\mathrm{d}T_\mu$ was analyzed using Eq. (6). The corresponding results are displayed in Fig. 5. In this figure, $f(\psi)$ of the RFG model is referred from [27]. The experimental data and neutrino flux $\Phi(E_\nu)$ are sourced from the MiniBooNE experiment [47]. In Fig. 5, we can observe that the three theoretical results can effectively reproduce the shape and positions of the peaks at different scattering angles. In addition, the flux-integrated differential cross sections all start from $T_\mu = 0$. This is because Eq. (6) accounts for all the incident neutrino energies, resulting in the outgoing muon kinetic energy starting from $T_\mu = 0$. Finally, the peak width of the scattering cross section narrows as $\cos\theta_\mu$ decreases. This narrowing is attributed to the momentum triangle relationship $q^2 = k^2 + k'^2 - 2kk'\cos\theta_\mu$ and momentum conservation in Eq. (13), where a smaller $\cos\theta_\mu$ results in a larger momentum transfer $q$, leading to a corresponding decrease in the maximum value of $T_\mu$.

After introducing *NN*-SRC, Fig. 5 clearly shows that when compared with the RFG and HFB models, the HFB+LFD model displays higher values and extends farther into the right tail of the cross section. This is because the other two models lack high-$p$ neutrons, with all states below the Fermi momentum $p_F$ being occupied. In addition, it can be observed that after introducing *NN*-SRC, the peak position of the flux-integrated differential cross section slightly decreases.

To more clearly extract the information about the neutron momentum distribution from the scattering cross section and analyze the influence of *NN*-SRC on the neutrino scattering, Fig. 6 presents the quasielastic $^{12}$C $(\nu_\mu,\mu^-)$ flux-integrated differential cross section $\mathrm{d}^2\sigma/\mathrm{d}\cos\theta\mathrm{d}T_\mu$ in logarithmic coordinates, with the scattering angle range of $0.2 \le \cos\theta_\mu \le 0.3$. As shown in Fig. 6, the HFB+LFD model, which incorporates the *NN*-SRC effects, yields larger values with an extended tail when compared with the results of the HFB model. This behavior can be explained through the scaling function $f(\psi)$ in Fig. 3. By combining the definition of $\psi$ in Eq. (10) and the energy conservation relation $T_\mu = E_\nu - \omega$, the negative-$\psi$ region in Fig. 3 corresponds to the high-$T_\mu$ region

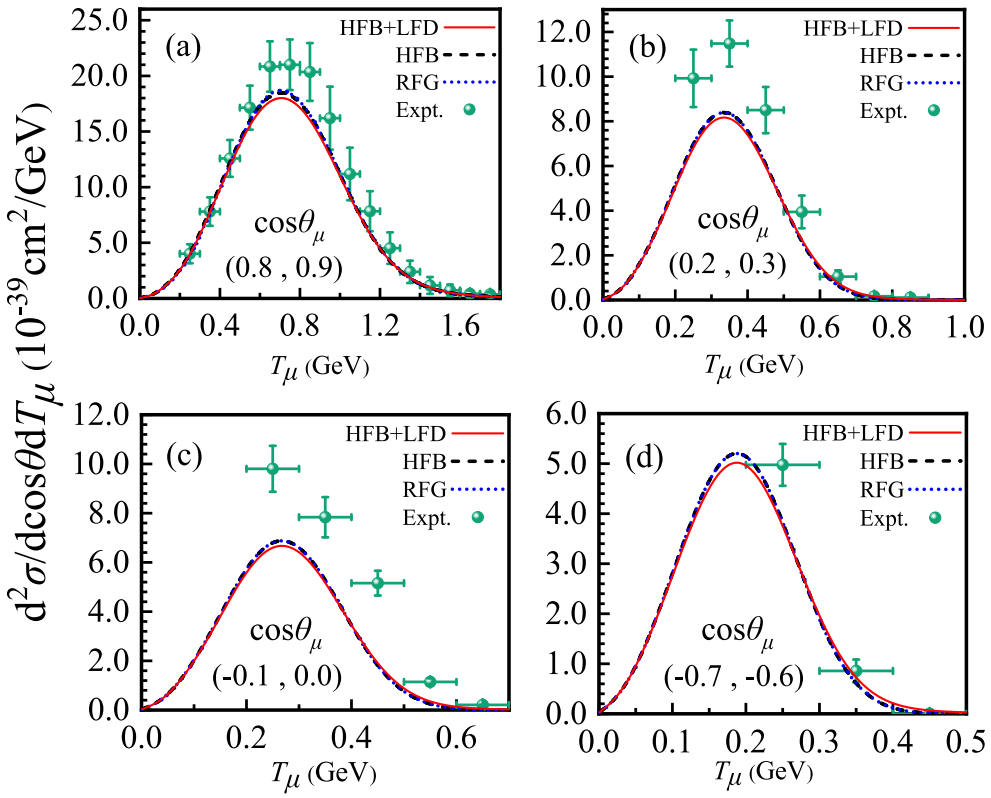


**Fig. 5.** (color online) Flux-integrated double-differential cross section per target nucleon for the CCQE process on $^{12}$C versus the muon kinetic energy $T_\mu$ for various bins of $\cos\theta_\mu$. The corresponding scaling functions $f(\psi)$ are obtained from the RFG, HFB, and HFB+LFD approaches. (a) $0.8 \le \cos\theta_\mu \le 0.9$, (b) $0.2 \le \cos\theta_\mu \le 0.3$, (c) $-0.1 \le \cos\theta_\mu \le 0.0$, (d) $-0.7 \le \cos\theta_\mu \le -0.6$.

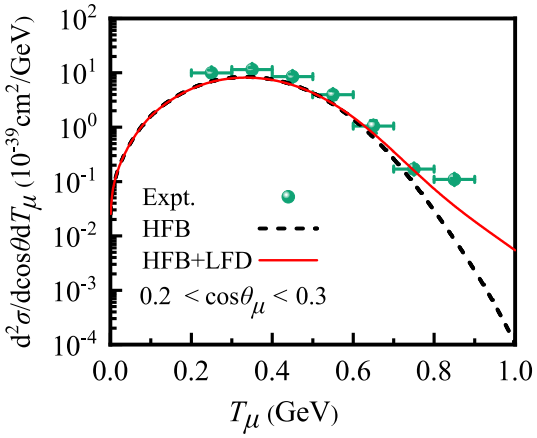


**Fig. 6.** (color online) Flux-integrated double-differential cross section per target nucleon in $^{12}$C versus muon kinetic energy $T_\mu$ in logarithmic coordinates, with the scattering angle range $0.2 \le \cos\theta_\mu \le 0.3$. In the calculation process, the correlation strength $C_A = 4.5$, which corresponds to 24% of neutrons above the Fermi momentum $p_F$.

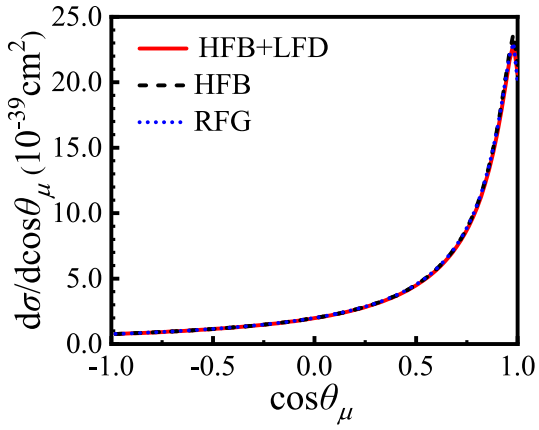


**Fig. 7.** (color online) Flux-averaged CCQE $\nu_\mu$-$^{12}$C neutrino scattering differential cross section per nucleon as a function of the muon scattering angle $\theta_\mu$.

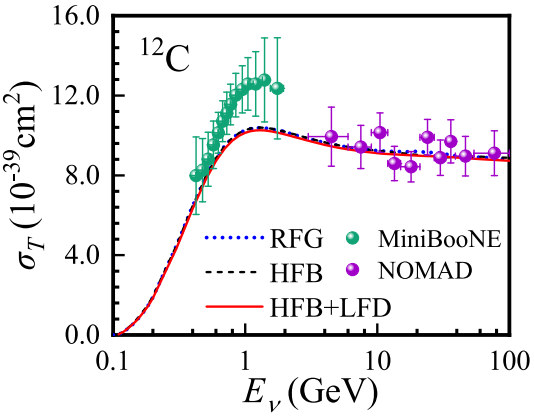


**Fig. 8.** (color online) CCQE $\nu_\mu$-$^{12}$C neutrino scattering total cross sections per nucleon versus reconstructed neutrino energy $E_\nu$, evaluated using the RFG, HFB, and HFB + LFD approaches. The experimental data are from MiniBooNE [47] and NOMAD [6] experiments.

of the scattering cross section. Because the *NN*-SRC effects predominantly influence the negative-$\psi$ region, the enhanced cross section observed in the high-$T_\mu$ region of Fig. 6 is directly attributable to these effects.

In Fig. 6, the HFB+LFD theoretical calculations incorporating the *NN*-SRC effects align well with the experimental values, exhibiting an upward trend at the right tail of the scattering cross section ($T_\mu > 0.6$ GeV). Furthermore, in Fig. 6, a comparison between the theoretical results and experimental data reveals that the *NN*-SRC strength is constrained to $C_A = 4.5$ in Eq. (19) for $^{12}$C. This exhibits an upward trend in the high-$T_\mu$ region of the scattering cross section and indicates that the correlated neutrons account for approximately 24% of the total neutron population. In this analysis, the contribution of the *NN*-SRC effects to the high-momentum neutrons in $^{12}$C is consistent with the *ab initio* calculation.

We continue to analyze the trend of the scattering cross section $\mathrm{d}\sigma/\mathrm{d}\cos\theta_\mu$ with respect to the variations in the outgoing muon angle $\theta_\mu$. Based on Eq. (8), the cross sections are represented as a function of the scattering angle $\theta_\mu$ by integrating over the incident neutrino energy $E_\nu$ and outgoing muon kinetic energy $T_\mu$. In Fig. 7, the cross sections $\mathrm{d}\sigma/\mathrm{d}\cos\theta_\mu$ from the three models are compared to analyze the effect of the neutron momentum distributions on the cross sections. This figure shows that scattering primarily occurs at small angles and is sensitive to the changes in $\theta_\mu$. Additionally, the results of the three models exhibit minimal differences in Fig. 7. This is because the scattering involves the same neutron number $\mathcal{N}$ but different NMDs. It is discernible that when compared with the NMDs, $\mathrm{d}\sigma/\mathrm{d}\cos\theta_\mu$ is more responsive to the neutron number $\mathcal{N}$ involved in the CCQE process.

Finally, the total cross section $\sigma_T$ of the CCQE neutrino scattering from Eq. (9) is investigated, and the results of $\sigma_T$ are presented in Fig. 8. In this figure, the blue, black, and red lines represent the total cross section calculated using the RFG, HFB, and HFB+LFD models, respectively. For comparison, the experimental data from MiniBooNE and NOMAD are also provided in this figure. As shown in Fig. 8, the shapes of the total theoretical cross sections $\sigma_T$ predicted by the three theoretical models agree well with the experimental data, which demonstrates the effectiveness of the scaling theory and reliability of the spectral function theory in Sec. II.

Three features are displayed in Fig. 8. First, the total cross section $\sigma_T$ begins at the reconstructed neutrino energy $E_\nu = 0.105$ GeV, which is because the minimum energy of the incident neutrinos must be sufficient to emit a muon with $m'_\mu = 0.105$ GeV. Second, in the region $0.105\ \mathrm{GeV} < E_\nu < 1\ \mathrm{GeV}$, the interaction between the

neutrinos and neutrons strengthens progressively, leading to a continuous increase in the value of $\sigma_T$. This can also explain the rise in the double-differential cross section $d^2\sigma/d\Omega' dT_\mu$ with increase in $E_\nu$ in Fig. 4. Finally, it can also be observed that in the region $E_\nu > 1$ GeV, $\sigma_T$ essentially stabilizes with increase in $E_\nu$. This indicates that the number of nucleons involved in the CCQE neutrino scattering reaches saturation.

We continue to compare and analyze the results from the three theoretical models. It is worth noting that after including *NN*-SRC, the difference in the total $\sigma_T$ between the HFB+LFD and HFB models becomes minor. This is also because the scattering cross sections are more sensitive to the neutron number rather than to the neutron momentum distribution. Therefore, after integrating over $\theta_\mu$ and $T_\mu$ for the different models in Fig. 4, the difference becomes negligible in the total cross sections. If we study the effects of *NN*-SRC through CCQE neutrino scattering, the flux-integrated cross section $d^2\sigma/d\cos\theta dT_\mu$ in Fig. 5 may present a more advantageous approach than the total cross section in Fig. 8.

The results in both Figs. 5 and 8 show a reduction in the flux-integrated and total cross sections for both the HFB and HFB+LFD methods when compared with the experimental values. This discrepancy primarily arises from the theoretical calculations not accounting for the two-nucleon knockout processes [7] and 2p-2h effect [48]. In the CCQE process, the occurrence of two-nucleon knockout increases the overall probability of the experimental scattering events. When neutrinos interact with groups of nucleons, such as proton-neutron pairs, the probability of neutrino-nucleus interactions is enhanced, resulting in an increased experimentally measured cross section. This phenomenon leads to theoretical results that are lower than the experimental data.

## IV. SUMMARY

In this study, we develop a theoretical model for CCQE neutrino scattering, which includes two primary components: the single nucleon scattering cross section $\sigma_0$ derived from the nucleon form factors, and the scaling function $f(\psi)$ obtained from the sophisticated nuclear structure model. Using the constructed scattering model, we analyze the behavior of the CCQE neutrino scattering cross sections at different scattering angles $\theta_\mu$ and incident neutrino energies $E_\nu$ to investigate the contributions of the MF and correlation nucleons.

The findings are summarized as follows. The flux-averaged differential cross sections show that the theoretical results can effectively reproduce the shape and positions of the peaks at different scattering angles. The neutron momentum distribution can be extracted from the cross sections, elucidating the *NN*-SRC effects on the neutrino-nucleus scattering. For the total cross section $\sigma_T$, the behavior of the scattering cross sections are analyzed across different reconstructed neutrino energy ranges. The starting point of the scattering cross sections occurs at $E_\nu = 0.105$ GeV. With increase in $E_\nu$, a turning point appears at $E_\nu = 1$ GeV. In the region $E_\nu > 1$ GeV, the total scattering cross section remains stable. This suggests that the number of nucleons participating in the CCQE neutrino scattering has achieved saturation.

The CCQE models in this paper can not only examine the nuclear structure models but can also be used to study the momentum distribution of the neutrons. The studies in this paper enhance our understanding of the nuclear structure and provide essential constraints for the analysis of signals and backgrounds in future neutrino oscillation experiments.

## References


[1] J. N. Bahcall, Rev. Mod. Phys. **59**, 505 (1987)
[2] T. Van, N. Jachowicz, R. Gonzalez-Jimenez *et al.*, Phys. Rev. C **94**, 024611 (2016)
[3] D. Akimov, J. Albert, P. An *et al.*, Science **357**, 1123 (2017)
[4] K. S. Kim, S. Choi, H. Gil *et al.*, Chin. Phys. C **48**, 084101 (2024)
[5] R. R. Rossi, G. Sanchez Garcia, and M. Trtola, Phys. Rev. D **109**, 095044 (2024)
[6] V. Lyubushkin, B. Popov, J. J. Kim *et al.*, Eur. Phys. J. C. **63**, 355 (2009)
[7] A. A. Aguilar-Arevalo, C. E. Anderson, A. O. Bazarko *et al.*, Phys. Rev. D **82**, 092005 (2010)
[8] P. Adamson, I. Anghel, A. Aurisano, *et al.*, Phys. Rev. D **91**, 012005 (2015)
[9] M. H. Ahn, S. Aoki, H. Bhang, Phys. Rev. Lett. **90**, 041801 (2003)
[10] N. Van Dessel, N. Jachowicz, R. Gonzalez-Jimenez, *et al.*, Phys. Rev. C **97**, 044616 (2018)
[11] A. M. Ankowski, Phys. Rev. C **86**, 024616 (2012)
[12] M. V. Ivanov, A. N. Antonov, J. A. Caballero, Phys. Rev. C **89**, 014607 (2014)
[13] J. A. Formaggio and G. P. Zeller, Rev. Mod. Phys. **84**, 1307 (2012)
[14] M. B. Barbaro, A. De Pace, T. W. Donnelly, *et al.*, Phys. Rev. C **98**, 035501 (2018)
[15] B. I. S. Van Der Ventel and J. Piekarewicz, Phys. Rev. C **69**, 035501 (2004)
[16] M. V. Ivanov, M. B. Barbaro, J. A. Caballero, *et al.*, Phys. Rev. C **77**, 034612 (2008)
[17] A. N. Antonov, M. V. Ivanov, J. A. Caballero, *et al.*, Phys. Rev. C **83**, 045504 (2011)
[18] P. Ring, Prog. Part. Nucl. Phys. **37**, 193 (1996)
[19] M. Bender, P.-H. Heenen, and P.-G. Reinhard, Rev. Mod. Phys. **75**, 121 (2003)
[20] V. L. Martinez-Consentino, A. M. Cantizani, and J. E.

Amaro, Phys. Rev. C **109**, 015502 (2024)
[21] P. R. Casale, J. E. Amaro, E. R. Arriola, *et al*., Phys. Rev. C **108**, 054001 (2023)
[22] Q. Niu, J. Liu, Y. Guo, *et al*., Phys. Rev. C **105**, L051602 (2022)
[23] O. Hen, M. Sargsian, L. B. Weinstein, *et al*., Science **346**, 614 (2014)
[24] J. Carbonell and V. A. Karmanov, Nucl. Phys. A **581**, 625 (1995)
[25] X. Wang, Q. Niu, J. Zhang, *et al*., Sci. China Phys. Mech. Astron. **64**, 292011 (2021)
[26] Y. Wang, X. Cao, J. Hu *et al*., Chin. Phys. C **49**(1), 014106 (2025)
[27] J. E. Amaro, M. B. Barbaro, J. A. Caballero *et al*., Phys. Rev. C **71**, 015501 (2005)
[28] J. E. Amaro, M. B. Barbaro, J. A. Caballero *et al*., Phys. Rev. C **71**, 065501 (2005)
[29] M. V. Ivanov, A. N. Antonov, M. B. Barbaro *et al*., Phys. Rev. C **91**, 034607 (2015)
[30] X. Lu, A. Abdukerim, Z. Bo, *et al*., Chin. Phys. C **48**(9), 091001 (2024)
[31] M. V. Ivanov and A. N. Antonov, Phys. Rev. C **109**, 064621 (2024)
[32] A. N. Antonov, M. K. Gaidarov, M. V. Ivanov *et al*., Phys. Rev. C **71**, 014317 (2005)
[33] C. CiofidegliAtti, E. Pace, and G. Salme, Phys. Rev. C **43**, 1155 (1991)
[34] L. Wang, Q. Niu, J. Zhang *et al*., Sci. China Phys. Mech. Astron. **66**, 102011 (2023)
[35] H. Wang, Q. Su, C. Xu *et al*., J. Phy. G: Nucl. Part. Phys. **50**, 095104 (2023)
[36] M. V. Ivanov, A. N. Antonov, G. D. Megias *et al*., Phys. Rev. C **99**, 014610 (2019)
[37] M. V. Stoitsov, N. Schunck, M. Kortelainen *et al*., Comput. Phys. Commun **184**, 1592 (2013)
[38] S. A. Kulagin and R. Petti, Nucl. Phys. A **765**, 126 (2006)
[39] C. Maieron and T. W. Donnelly, Phys. Rev. C **65**, 025502 (2002)
[40] A. N. Antonov, M. K. Gaidarov, M. V. Ivanov *et al*., Phys. Rev. C **65**, 024306 (2002)
[41] T. W. Donnelly and I. Sick, Phys. Rev. Lett. **82**, 3212 (1999)
[42] J. E. Amaro, M. B. Barbaro, J. A. Caballero *et al*., Phys. Rev. Lett. **108**, 152501 (2012)
[43] G. D. Megias, J. E. Amaro, M. B. Barbaro *et al*., Phys. Rev. D **94**, 093004 (2016)
[44] A. M. Ankowski, O. Benhar, C. Marianio *et al*., Phys. Rev. D **93**, 113004 (2016)
[45] V. L. Martinez-Consentino, J. E. Amaro, P. R. Casale *et al*., Phys. Rev. D **108**, 013007 (2023)
[46] A. De Pace, M. Nardi, W. M. Alberico *et al*., Nucl. Phys. A **741**, 249 (2004)
[47] A. A. Aguilar-Arevalo, C. E. Anderson, A. O. Bazarko *et al*., Phys. Rev. D **81**, 092005 (2010)
[48] J. E. Sobczyk, J. Nieves, and F. Sanchez, Phys. Rev. C **102**, 024601 (2020)